Non-destructive wafer-level bond defect identification by Scanning Acoustic Microscopy

S. Brand, S. Tismer, S.T. Moe, K. Schjølberg-Henriksen

Abstract

Metal-based thermocompression bonding enables the creation of hermetic seals formed at relatively low processing temperatures and occupying a small portion of the device area. In the current study we have investigated the application of scanning acoustic microscopy (SAM) for assessing the quality of metal thermocompression bonds, both by evaluating its capabilities of localizing areas of poor bonding, and by finding defects in the integrity of the bond seal. Wafer laminates containing a test vehicle with pre-defined defects in the bond metal layer were sealed by Au-Au and Al-Al thermocompression bonding. Employing SAM, an area of 5 chips of poor bonding was identified non-destructively on the Al-Al laminate. Line defects of width 3.6 μm and point defects of diameter 22.4 μm have also been identified by SAM. The dicing yield for sealing frames was above 96% for all frame structures and both bond metal systems. The average bond strength was 31.5 ± 11.9 MPa for Al-Al thermocompression bonds and 37.3 ± 9.7 MPa for Au-Au thermocompression bonds. Scanning acoustic microscopy operates non-destructively and proved to be an extremely useful tool complementing current state-of-the-art methods for bond quality assessment.

Introduction

Encapsulation and packaging of micro-electro-mechanical-systems (MEMS) accounts for more than 70% of the device cost (Reich and Grossner 2001). Wafer-level bonding has the potential to significantly reduce packaging costs, and is extensively used in the fabrication of for instance pressure sensors (Aono *et al.* 2011) and inertial sensors (Knechtel 2010).

A variety of different bonding technologies are currently applied in packaging of commercial MEMS devices. Glass frit bonding (Knechtel 2005; Knechtel 2010), anodic bonding (Wallis and Pomerantz, 1969; Aono *et al.* 2011), and high-temperature direct silicon fusion bonding (Tong and Gösele 1999; Nese and Seeberg 2006) have been used in commercial products for a long time. Since recently, metal thermocompression bonding is increasingly applied as a wafer-level packaging technology. The company ST Microelectronics has reduced the area used for device sealing by using Au-Au thermocompression bonding instead of the conventional glass frit bonding as described by Fraux and Baron (2011). The company Analog Devices has investigated the potential of Al-Al thermocompression bonding for application in MEMS encapsulation (Martin 2007; Yun *et al.* 2008).

The yield of bonding processes greatly influences the device cost. Therefore, the identification and subsequent elimination of the root-causes of occurring defects is of major concern at this stage of device processing. The fact that glass is optically transparent, strongly simplifies the inspection and thus the detection of defects occurring during anodic

bonding processes. Ultrasonic inspection, however, employs acoustic waves to non-destructively inspect internal structures and compositions in optically opaque materials. The use of highly focused pressure waves allows a distinct and highly resolved visualization of the integrity of functional structures in microelectronic components. Brand *et al.* (2010) have used acoustic microscopy to non-destructively inspect and evaluate flip-chip contacts. Besides a pure visualization of those interconnects, information about the integrity and functionality of the flip-chip contacts have been derived from the reflected ultrasonic signals in an automated manner and proved superior to a complementary X-ray inspection by even highly trained technicians. Naumann *et al.* (2013) have shown the high value of scanning acoustic microscopy (SAM) for non-destructively assessing the quality of glass-frit bonds, predicting the conditions of micro-chevron-test samples.

The waves received in an acoustic microscope carry the information about the interaction with physical structures encountered during the propagation through the sample (Briggs 1995). Therefore, specific characteristics of the acquired signals can be extracted and correlated with the physical condition of the inspected specimen. The phenomena applied in an acoustic microscope are based on the propagation of elastic waves that interact with the mechanical properties of the materials and interfaces encountered during their propagation path. By acoustic inspection, gradients of mass density and sound velocity are assessed and can be evaluated quantitatively, since the sound velocity represents the materials elastic properties. This fact leads to an increased reflectivity at boundaries between materials with differing mechanical and elastic properties. A direct relationship between this gradient, the elastic properties of the neighboring materials, and the signal amplitude received can be observed. Therefore, inclusions of gaseous materials, as in the case of a delamination of

bonded materials, can easily be assessed by an acoustic inspection. Such gaseous inclusions may not be noticed by an X-ray inspection, due to the absence of an absorption contrast of gaseous layers. Since acoustic waves directly interact with the mechanical material properties, SAM can be employed in a large variety of applications (Brand 2011).

In the current paper, we have investigated SAM as a method for evaluation of bond quality of metal thermocompression bonded seals. Test wafer laminates with chips containing sealing frames relevant for MEMS device encapsulation were fabricated. Defect structures were intentionally introduced in the metal sealing frames prior to the bonding process. The ability of SAM to find the intentionally introduced bonding defects and areas of poor bonding is reported. A correlation of the results obtained by SAM and conventional bond quality assessment like dicing yield, bond strength, and visual inspection of fractured bond interfaces has been performed and is presented here.

Materials and Methods

Sample Preparation

Wafer laminates were prepared by joining a top and a bottom wafer. The top wafers complied with SEMI standard and were 400 μm thick, double side polished, p-type of orientation <100>, and of 150 mm diameter. A pattern of frames protruding 6 μm above the wafer surface was formed by deep reactive ion etching (DRIE) using patterned SiO_2 as masking material. The pattern contained frames with outer dimension 3 × 3 mm^2 and of width 100, 200, or 400 μm, named F100, F200, and F400. One frame of width 200 μm with rounded corners, named F200R, was also included. The designs and their bond areas are listed in Table 1. In addition to the frames, other minor structures were included on the

wafer, so that the total bond area was 525 mm^2. On the backside of the top wafer, identification marks were placed to identify the individual chips after bonding.

The bottom wafers were of 700 µm thickness and single side polished. Both top and bottom wafers were stripped of all SiO$_2$ prior to deposition of the bonding metal layer. In the current study, two different bonding metals were employed: Au-Au thermocompression bonding and Al-Al thermocompression bonding. For the Au-Au thermocompression bonding, 0.2 µm TiW and 1.0 µm Au was sputter deposited on both the top and bottom wafer. For the Al-Al thermocompression bonding, 1.0 µm Al was sputter deposited on both the top and bottom wafer.

After sputtering, the metal of the bottom wafer was patterned, defining bond areas with intentional line and point defects of five different defect sizes S1 – S5 ranging from 3.6 – 56.2 µm. Line defects and square point defects of all five sizes were made. The resulting sizes of the defects S1 – S5 on the Au and Al wafer were measured by scanning electron microscopy prior to bonding, and are listed in Table 2. Figure 1 shows the bond areas of the top and bottom wafers and the intentional defects. Figure 2 shows a schematic top view and cross-section of a bonded die with intentional defects.

The two laminates were bonded in a SB6e (Suss MicroTec, Garching, Germany) substrate bonder. Bond parameters at the edge of the process window were applied intentionally to create variations in the bond quality across the entire laminate. The Au laminate was bonded in a chamber pressure below 10^{-3} mbar, applying a tool pressure of 2 bar for 15 minutes at 350 °C. The applied tool pressure translated to a pressure of 8.5 MPa on the

protruding bond area. The Al laminate was bonded in a chamber pressure below 10^{-3} mbar, applying a tool pressure of 5 bar for 60 minutes at 500 °C. The applied tool pressure translated to a pressure of 21.2 MPa on the protruding bond area.

Scanning Acoustic Microscopy

The two bonded wafer laminates were inspected by scanning acoustic microscopy at 175 MHz ultrasonic frequency employing two different focal lengths. The transducer used for overview imaging of the entire wafers had a focal length of 8 mm (V3955 Panametrics, Waltham, USA). Another ultrasonic transducer was used for high resolution imaging of individual sample chips, having a focal length of 4 mm (175-4, PVA TePla Analytical Systems GmbH, Westhausen, Germany) The acoustic microscope employed here was an Evolution II (PVA TePla Analytical Systems GmbH, Westhausen, Germany). Due to the high reflectivity at the front of the acoustic lens and at the surface of the sample, a coupling medium was required for scanning and matching the acoustic impedances of both materials. De-ionized and de-gassed water at 21^oC was used as coupling medium.

To optimize the acoustical imaging within solid samples, the focus of the ultrasonic transducer has to be carefully placed at the bonding interface inside the sample. Insonation for overview imaging was performed through the wafer of 700 μm thickness, applying the 8 mm transducer and a scan increment of 38.6 μm. High resolution imaging using the 4 mm focal length transducer however, was performed through the wafer of 400 μm thickness, at a 7.4 μm scan increment. In the authors' experience, an imaging resolution of approximately 10 – 20 μm is possible through 400 μm of Si at 175 MHz.

The two ultrasonic transducers had different advantages. The 4 mm transducer had higher resolution capability due to its larger opening angle and the reduced imaging depth due to the smaller radius of curvature of the transducers calotte, compared to the transducer with 8 mm focal length. The 8 mm transducer on the other hand was less susceptive to the wafer bow, the corresponding defocussing of the transducer, and the occurring interference fringes caused by the superposition of the interface echo and a potential delay-line echo signal (i.e. internal transducer reflection). Prior to acoustic data acquisition, reflected acoustic signals were pre-amplified by 42 or 48 dB by the internal RF unit of the acoustic microscope.

Received echo signals have been digitized at a sampling rate of 1 GS/s with a resolution of 8 bit and stored on the microscope's internal hard disc drive and were transferred to a workstation computer for additional off-line analysis. The subsequent signal processing of the acoustical data was performed using SAMNALYSIS (Fraunhofer IWM, Halle and PVA TePla Analytical Systems GmbH, Westhausen, Germany). SAMNALYSIS is a software toolbox based on MATLAB (The Mathworks, Natick, USA). SAMNALYSIS provides a large variety of signal- and data processing algorithms for quantitative and qualitative parametric imaging and evaluation of acoustical signals. Acquired ultrasonic echoes were transferred into the frequency domain using the Fast-Fourier transform provided by MATLAB. The power spectra computed from the Fourier transform were then split into individual frequency containers of 5 MHz band width, integrated, and further subjected to a split-spectrum intensity mapping. Imaging in the frequency domain allows for an increase in the lateral resolution and enables an optimized sensitivity to the bond quality related parameters.

Dicing Yield and Destructive Pull Testing

After SAM investigation, the laminates were diced into individual chips of size 6 × 6 mm^2. The dicing yield was calculated as the percentage of chips that were not delaminated during the dicing process. Subsequently, selected chips were pull tested using a MiniMat 2000 (Rheometric Inc., Epsom, United Kingdom). Eight chips of design F200R from each laminate were subjected to pull-testing to quantitatively estimate the bond strength. In addition, 20 chips that had been investigated by SAM were pull-tested to compare the fractured surfaces with the acoustic results. In preparation to pull-testing, individual chips were glued to flat-headed screws which were mounted in the Minimat 2000. During the pull test, the elongation of the sample versus the applied force was recorded. The force at which the fracture of the sample occurred was noted. The bond strength was then calculated as the fracture force divided by the nominal bonded area. After pull testing, the fractured surfaces were inspected using a stereo microscope at 10-fold magnification. The fractures were then classified as either cohesive or adhesive, and the material(s) of the cohesive and adhesive fractures were determined by visual inspection.

Results

Scanning Acoustic Microscopy

Figure 3 and Figure 4 show SAM overview images of the entire Al-Al laminate and the Au-Au laminate. The imaging contrast was higher for the Al-Al laminate (Figure 3) than for the Au-Au laminate (Figure 4). The internal pre-amplification was reduced from 48 dB for the Al-Al laminate to 42 dB for the Au-Au laminate in order to improve the visibility of the smaller delamination defects. The acoustic micrographs of the entire laminates identified areas with potentially poorly bonded areas in the center of the Al-Al laminate, as shown in Figure 3.

Figures 5 – 8 show acoustic detail micrographs of chips from the Al-Al laminate. Figure 5 indicates the improved imaging resolution achieved by the split-spectrum analysis. Figure 6 also shows the results of the narrow-band spectral imaging and allows the identification of the intentionally introduced bonding line defects of 3.6 µm width. The line defects of widths 4.5, 7.2, 22.4, and 52.3 µm can also clearly be seen, as well as the point defects of 22.4 µm and 52.3 µm. In Figures 7 and 8, a varying imaging contrast can be identified in the bond frames, indicating a change in acoustic reflectivity which is likely to be related to the condition of the bond seal. Figures 9 – 10 contain acoustic detail micrographs of two selected chips from the Au-Au laminate sample. While Figure 9 shows a chip with a well bonded frame, Figure 10 displays a chip with several poorly bonded areas in the bond frame.

Fracture Surfaces

Inspection of the fracture surfaces after pull testing of chips bonded by Al-Al thermocompression bonding showed that all chips except chip 208 had cohesive fracture in both the silicon and the aluminum seal. Chip 208, of design F100, showed cohesive fracture in the aluminum only. For the other chips, the amount of cohesive silicon fracture ranged from less than 2% to 80%. The three chips with a fracture force below 5 N all had less than 2% cohesive silicon fracture. Figure 11 shows optical micrographs of fracture surfaces of chips from the Al-Al laminate. The chips in Figure 11 are the same chips as in the acoustic micrographs in Figures 5, 7, and 8.

The chips bonded by Au-Au thermocompression bonding all exposed three types of fracture simultaneously: cohesive silicon fracture, cohesive gold fracture, and adhesive fracture at

the interface between TiW and Si. Optical micrographs of the fracture surfaces of the chips from Figures 9 – 10 are displayed in Figure 12.

Dicing Yield, Bond Strength and Fracture Types

The dicing yield for each frame design is plotted in Figure 13. A dicing yield above 96% was obtained for all chip types, regardless of frame width. There was no significant difference between Au-Au and Al-Al bonding with respect to dicing yield. The average values and standard deviations for the fracture forces and bond strengths calculated from eight measured chips are listed in Table 3. The average fracture forces were 79.9 N for Au-Au bonds and 67.4 N for Al-Al bonds. However, student t-testing showed that the bond strengths were not significantly different, even at only 90% confidence level.

Discussion

The acoustical overview image shown in Figure 3 enabled the detection of approximately 5 chips with poor metal thermocompression bonding in the center of the laminate. The poorly bonded area in the center of the Al-Al laminate was discernible by SAM prior to device dicing, when the poorly bonded chips delaminated. No such areas of poor metal bonding were seen in the acoustic micrograph the Au-Au laminate (Figure 4), and no large areas with delaminated chips occurred during dicing, suggesting that thermocompression bonds that were too weak to withstand dicing could be identified by SAM.

The acoustic micrographs in Figure 5 – Figure 10 show that line defects as narrow as 3.6 μm could be detected by SAM supplemented by appropriate signal processing, and that point

defects of diameter 22 μm could also be seen. The detected point defect size was in agreement with the expected resolution of 10 – 20 μm through 400 μm silicon material. The detected line defect size was considerably smaller than the expected resolution. It is assumed that the successful detection of the narrow lines, even though 400 μm of silicon material, was due to the high acoustic reflectivity at solid / gaseous interfaces. It should be noted that there is a discrepancy between the detection limit and the resolution limit when acoustically inspecting debonds in laminated wafers. Gaseous inclusions between solid interfaces cause an extreme reflectivity (R≈1) that can be detected acoustically even though its lateral dimensions are below the actual resolution limit. This can be explained by the convolution of a small spot of extreme reflectivity with the much larger acoustical beam. This also causes the defect to appear much larger than it actually is.

The pull tested chips showed various types of fracture surfaces: these were adhesive fractures and cohesive fractures in the bulk silicon and in the bond metal. Cohesive fracture surfaces in the bulk silicon indicate that the bonded interface has a strength comparable to that of bulk silicon. However, cohesive fracture interface in the bond metal does not describe the bond strength, since it can occur in both strong and weak bonds. Therefore, interpretation of fracture surfaces does not always imply an assessment of the strength of thermocompression bonds. By comparing the scanning acoustic micrographs in Figures 5 – 10 and the fracture surfaces in Figures 11 and 12, it is evident that chips with very similar appearance of the fracture surfaces were shown to be very different by SAM.

The average bond strengths listed in Table 3 were similar to or higher than the strengths reported in earlier studies (Taklo *et al.* 2004; Kurotaki *et al.* 2008; Schjølberg-Henriksen *et al.*

2012; Malik *et al.* 2013). The large standard deviations of the fracture force distributions imply that no clear conclusion can be made regarding which of the two investigated bonding metals that resulted in the highest strength. However, a high bond strength value does not necessarily mean that a tight seal has been formed along the length of the entire bond frame. For instance chip No 17 in Figure 4 clearly showed areas that were not bonded at all, but still had a fracture force of 39.3 N (33.9 MPa).

In some of the fractured samples, the bonding Al had a deviating color in a part of the bonded frame. Chip 17 in Figure 11 is one example. The areas of the bonding Al with deviating color are thought to mark drying stains in areas of the bond frames, i.e. indications of water leaking across the bond frame, and hence, a poor seal. This assumption is supported by the acoustic micrograph of the same chip (Figure 5), which does indicate a poor bond in that particular area. In other samples, like chip 146 (Figure 11), a deviating color was observed on the silicon surface near the corners of the bond frame. The scanning acoustic micrographs (see Figure 5) also showed that the area near the corners of the bond frame seem to be different. It is assumed that during SAM, the areas near the corners of the bond frames were showed air bubbles caused by incomplete filling of coupling medium in the volumes enclosed by the frames. These areas are thought to be visible in the fracture surfaces due to drying stains.

In summary, SAM was found to be a non-destructive technique that complemented other available tools for assessing bond quality. SAM could identify wafer areas that were not likely to withstand wafer dicing, and line and point defects at the bonded interface. SAM also showed to be useful in the assessment of bond hermeticity.

Conclusions

Structured silicon wafers were joined by Al-Al and Au-Au thermocompression bonding. The bonding metal contained intentionally introduced line and point defects of sizes ranging from 3.6 µm to 56.2 µm. Areas with poor bonding, line defects of width 3.6 µm, point defects of a size down to 22 µm, and non-hermetic bonds were identified by non-destructive scanning acoustic microscopy inspection through 400 µm thick silicon material. The dicing yield for sealing frames was above 96% for frame widths 100 – 400 µm and for both bond metals. The average bond strength was 31.5 ± 11.9 MPa for Al-Al thermocompression bonds and 37.3 ± 9.7 MPa for Au-Au thermocompression bonds. Scanning acoustic microscopy proved to be a powerful tool complementing other bond quality assessment tools, like dicing yield count, bond strength measurements, and investigation of fracture surfaces.

Acknowledgements

References

Aono T, Suzuki K, Koide A, Jeong H, Degawa M, Yamanaka K, Hayashi M (2011) Wafer-level two-step bonding process for combined sensor with two different pressure chambers. *Proc 16th International Solid-State Sensors, Actuators and Microsystems Conference*, *TRANSDUCERS*

Brand S, Czurratis P, Hoffrogge P, Petzold M (2010) Automated inspection and classification of flip-chip-contacts using scanning acoustic microscopy. Microelectronics Reliability 50(9-11):1469-1473

Brand S, Czurratis P, Hoffrogge P, Temple D, Malta D, Reed J, Petzold M (2011) Extending acoustic microscopy for comprehensive failure analysis applications. Journal of Materials Science in Electronics, 22(10):1580-1593

Briggs A (1995) Advances in Acoustic Microscopy. Plenum Press, New York

Fraux R, Baron J (2011) STMicroelectronics' innovation in wafer-to-wafer bonding techniques shrinks MEMS die size and cost! 3D Packaging, No 21, November

Knechtel R (2005) Glass frit bonding: An universal technology for wafer level encapsulation and packaging. Microsystem Technologies 12(1-2): 63-68

Knechtel R (2010) Single crystalline silicon based surface micromachining for high precision inertial sensors: technology and design for reliability. Microsystem Technologies 16(5): 885 – 893

Kurotaki H, Shinohara H, Kobayashi H, Mizuno J, Shoji S (2008) Study of low-temperature wafer bonding with Au-Au bonding technique. Proc MicroNano, Kowloon, Hong Kong, June 3-5

Malik N, Schjølberg-Henriksen K, Poppe E, Taklo MMV, Finstad TG (2014) Al-Al thermocompression bonding for wafer-level MEMS packaging. Sensors and Actuators A, in press

Martin J (2007) Wafer-capping of MEMS with fab-friendly metals. Proc. SPIE 6463: 64630M1-6

Naumann F, Brand S, Bernasch M, Tismer S, Czurratis P, Wünsch D, Petzold M (2013) Advanced characterization of glass frit bonded micro-chevron-test samples based on scanning acoustic microscopy. J Microsyst Technol, 19(5):689-695

Nese M, Seeberg BE (2006) Silicon MEMS pressure sensors for aerospace applications. Proceedings of MNT for Aerospace Applications, CANEUS

Reichl H, Grosser V (2001) Overview and development trends in the field of MEMS packaging. Proc. IEEE MEMS Conference, Interlaken, Switzerland, January

Schjølberg-Henriksen K, Moen AS, Fasting E, Poppe E (2012) Yield and strength of metal wafer-level MEMS device sealing using Al, Au, or Ti. Proceedings of the SMTA International Wafer Level Packaging Conference, San Jose, CA, November 7 – 8

Taklo MMV, Storås P, Schjølberg-Henriksen K, Hasting HK, Jakobsen H (2004) Strong, high-yield and low-temperature thermocompression silicon wafer-level bonding with gold. Journal of Micromechanics and Microengineering 14: 884 – 890

Tong QY, Gösele U (1999) Semiconductor Wafer Bonding. John Wiley & Sons, New York

Wallis G, Pomerantz DI (1969) Field-assisted glass-metal sealing. Journal of Applied Physics 40: 3946 – 3949

Yun CH, Martin JR, Chen L, Frey T (2008) Clean and conductive wafer bonding for MEMS. Book of Abstracts 214th Electrochemical Society Meeting, Abstract No 2232

Table 1: The four designs of the protruding bond frames.

Chip ID	Description	Bond area [mm^2]	Number of chips on wafer
F100	Frame, width 100 µm, straight corners	1.16	54
F200	Frame, width 200 µm, straight corners	2.24	54
F200R	Frame, width 200 µm, rounded corners	2.14	54
F400	Frame, width 400 µm, straight corners	4.16	54

Table 2: Defect sizes S1 – S5 on the Al and Au wafers. The sizes describe the width of the line defects and the side edge of the square point defects.

Defect size ID	Line defect width/ side edge of square point defect [µm]	
	Al	Au
S1	3.6 ± 1.0	8.0 ± 2.0
S2	4.5 ± 1.0	8.2 ± 2.0
S3	7.2 ± 1.0	10.2 ± 2.0
S4	22.4 ± 1.0	25.3 ± 2.0
S5	52.3 ± 1.0	56.2 ± 2.0

Table 3: Measured fracture force and bond strength of the two laminates. The numbers are average values and standard deviations of eight measured chips of design F200R.

Laminate	Fracture Force [N]	Bond strength [MPa]
Al-Al	67.4 ± 25.4	31.5 ± 11.9
Au-Au	79.9 ± 20.7	37.3 ± 9.7

Figure 1: Top view of the protruding frames on the top wafer (left) and the bond metal pattern on the bottom wafer (right). The inset to the right shows the intentional metal defects in the bond metal. The wafers are bonded in areas the where the protruding frames and the bond metal are both present.

Figure 2: Schematic top view and cross-section along A-A' of a bonded frame die with intentional defects.

Figure 3: Acoustic micrograph of the entire Al-Al laminate, inspected at 175 MHz with a transducer with 8 mm focal length, applying 48 dB pre-amplification. The SAM was performed through 700 µm thick silicon material. The white ellipse indicates an area of approximately 5 poorly bonded dies in the center of the laminate.

Figure 4: Acoustic micrograph of the entire Au-Au laminate, inspected at 175 MHz with a transducer with 8 mm focal length, applying 42 dB pre-amplification. The SAM was performed through 700 μm thick silicon material.

Figure 5: Acoustic micrographs of chip No 17 of type F100 from the Al-Al laminate, inspected at 175 MHz frequency applying 8 mm focal length, 48 dB pre-amplification and 7.4 μm scan increment. Left: conventional SAM imaging. Right: after transferring the time-domain signals into the spectral domain. The white arrows indicate poor bonding and possible leak in an area of the bonded frame. The black arrow indicates possible trapped air.

Figure 6: Acoustic micrograph of chip of type F200 from the Al-Al laminate, inspected through 400 μm thick silicon material at 175 MHz frequency applying 4 mm focal length, 33 dB pre-amplification and 7.2 μm scan increment. All line defects, including those of width 3.6 μm are seen, in addition to individual point defects of side edge 22.4 and 52.3 μm.

Figure 7: Acoustic micrograph of chip No 146 of type F200R from the Al-Al laminate, showing that approximately 40% of the frame was poorly bonded.

Figure 8: Acoustic micrographs acquired through 700 μm silicon material at 175 MHz with 8 mm focal length. Left image: Acoustic micrographs of chip No 54 of type F400 from the Al-Al laminate. Line and point defects of size 22.4 and 52.3 μm are clearly seen. There is no indication of poorly bonded areas. Right image: Acoustic micrograph of chip No 21 of type F400 from the Al-Al laminate. All line defects are seen, as well as point defects of size 52.3

µm. There may be some indication of poorly bonded areas between defects S3 – S5 and around defects of size S2.

Figure 9: Acoustic micrograph of chip No 31 of type F200R from the Au-Au laminate obtained through 700 µm silicon material at 175 MHz with 8 mm focal length. All line defects and point defects of size 56.2 µm can be seen. There is no indication of poorly bonded areas.

Figure 10: Acoustic micrograph of chip 6 of type F200R from the Au-Au laminate scanned through 400 µm silicon material. All line defect sizes and point defects of sizes 25.3 and 56.2 µm can be seen. The chip seems to have poorly bonded areas on each of the four edges.

Figure 11: Fracture surfaces of chips 17 (type F100), 54 (type F400), and 146 (type F200R) from the Al-Al laminate. Both fracture surfaces are shown. The arrow in chip No 17-1 points to an area where the Al bond frame had a deviating color. The arrow in chip No 146-1 indicates an area where the enclosed silicon surface had a deviating color.

Figure 12: Fracture surfaces of chips No 6 and 31 of type F200R from the Au-Au laminate.

Figure 13: The dicing yield of the four bond frame types for the two bonded laminates.

Figure 01
Click here to download high resolution image

Figure 02

A - A'

Top wafer

Bottom wafer

Bond metal

Bond interface

Intentional defects
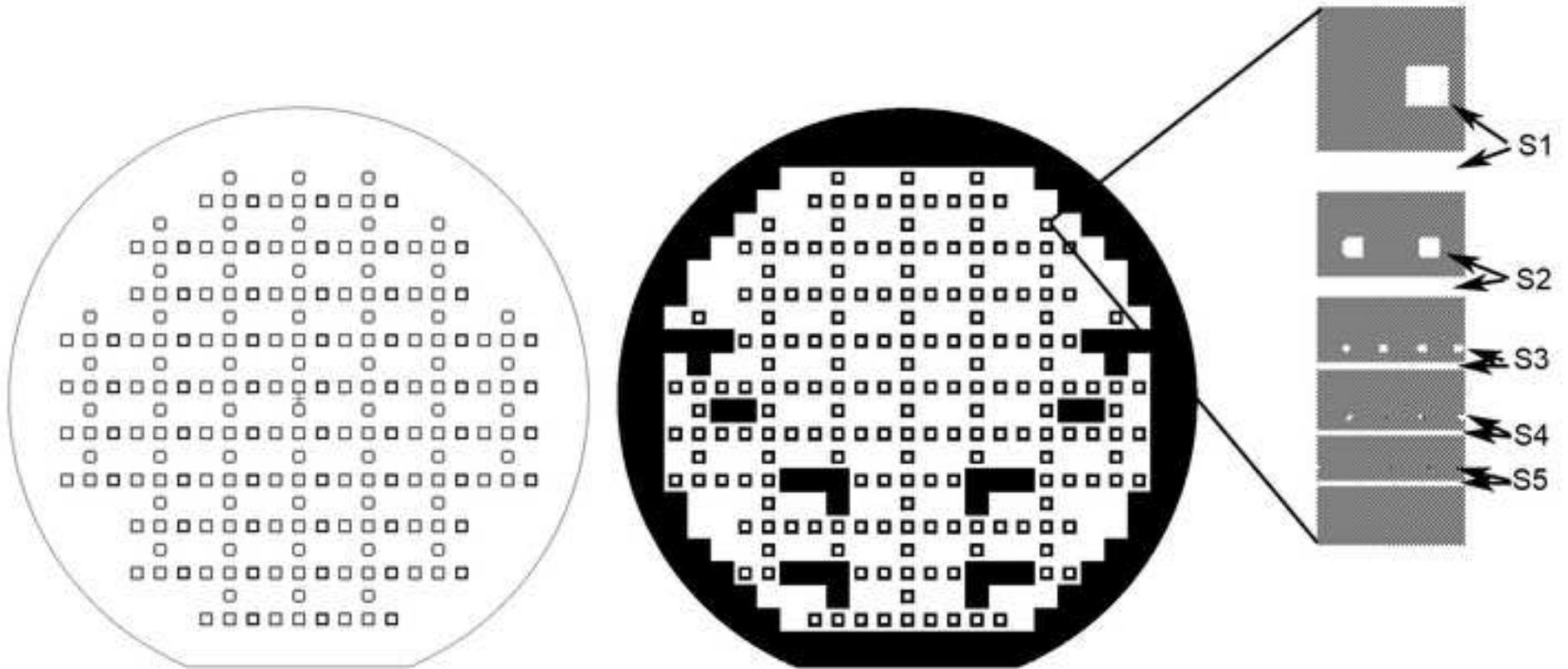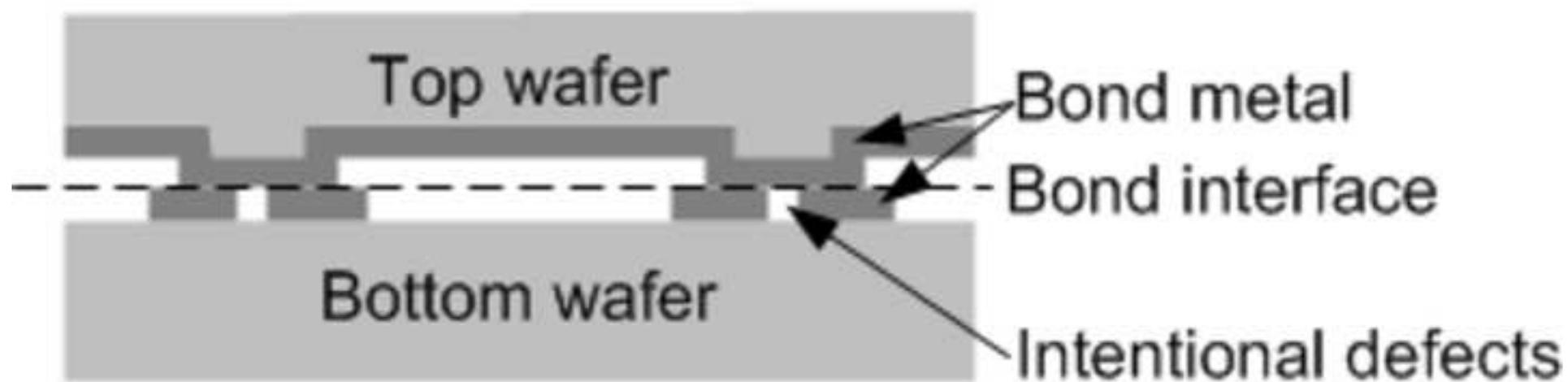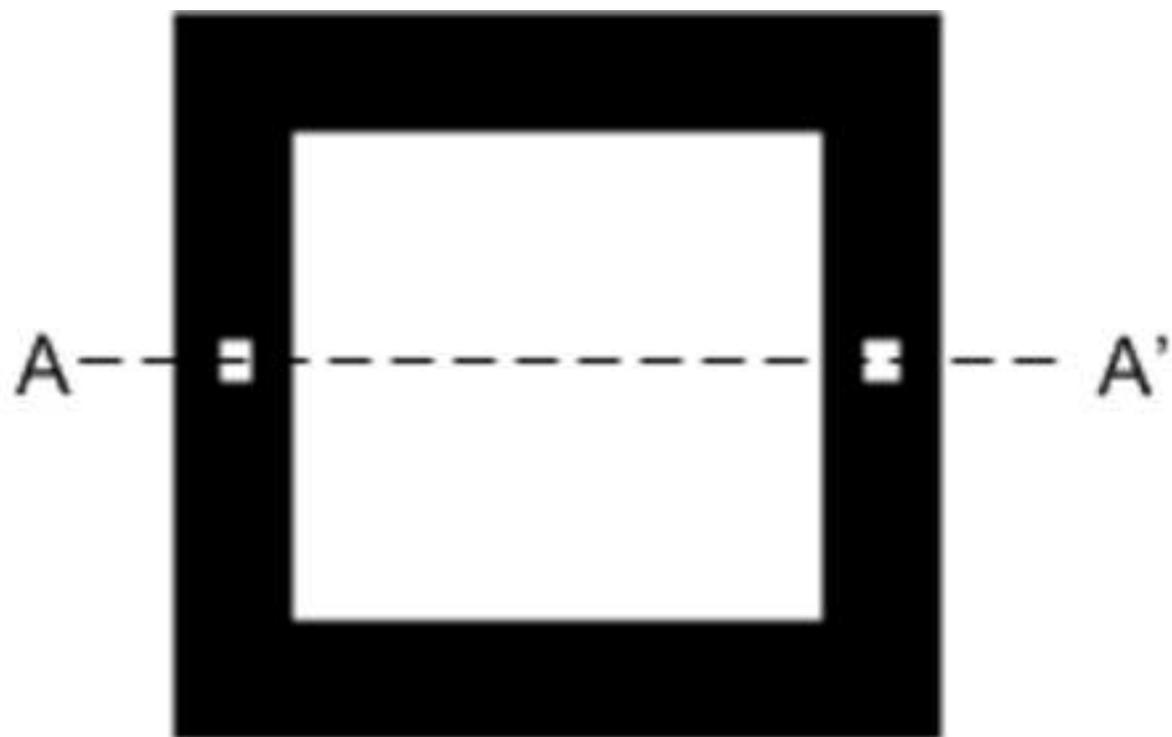
Figure 03
Click here to download high resolution image
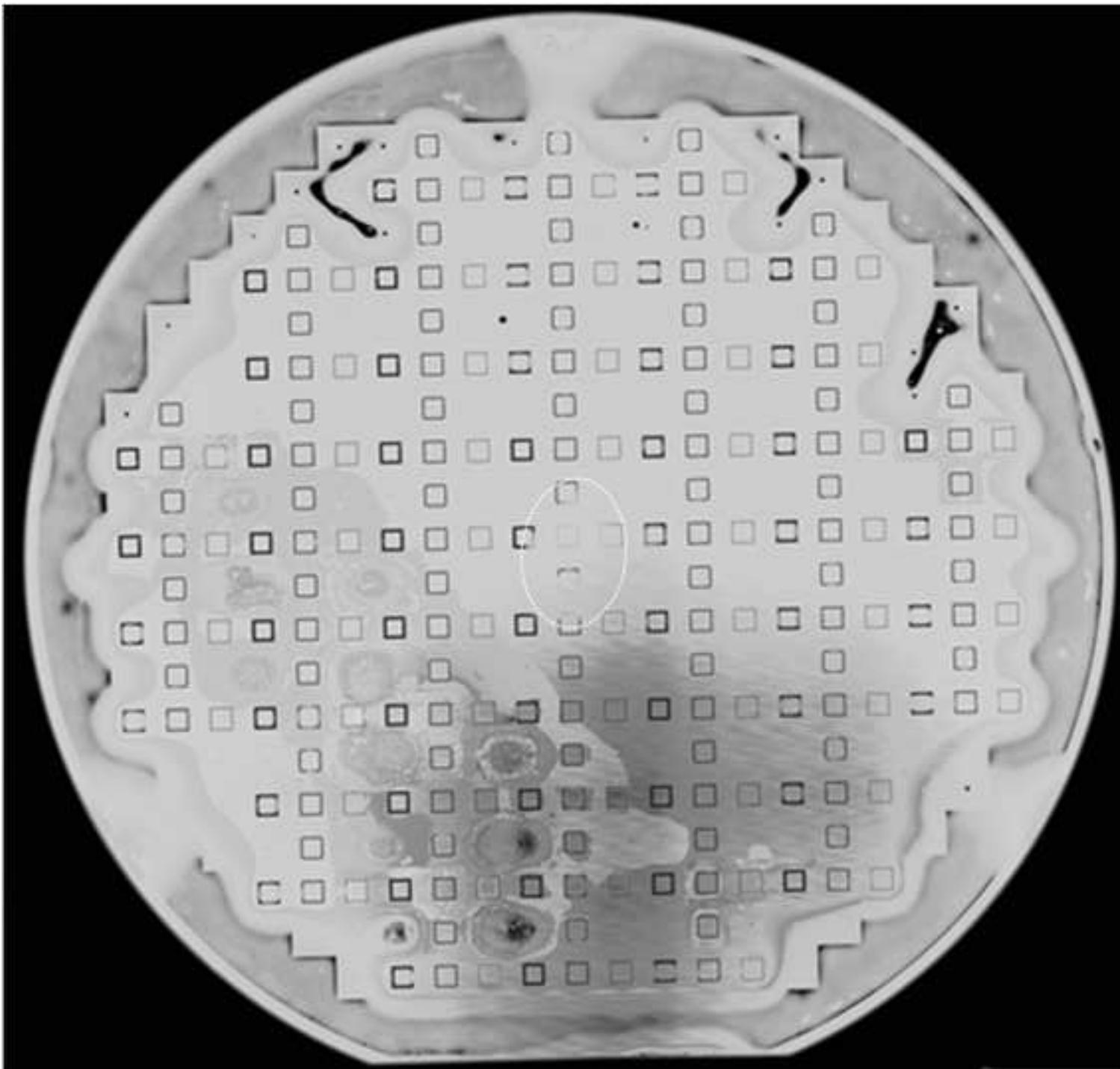
Figure 04
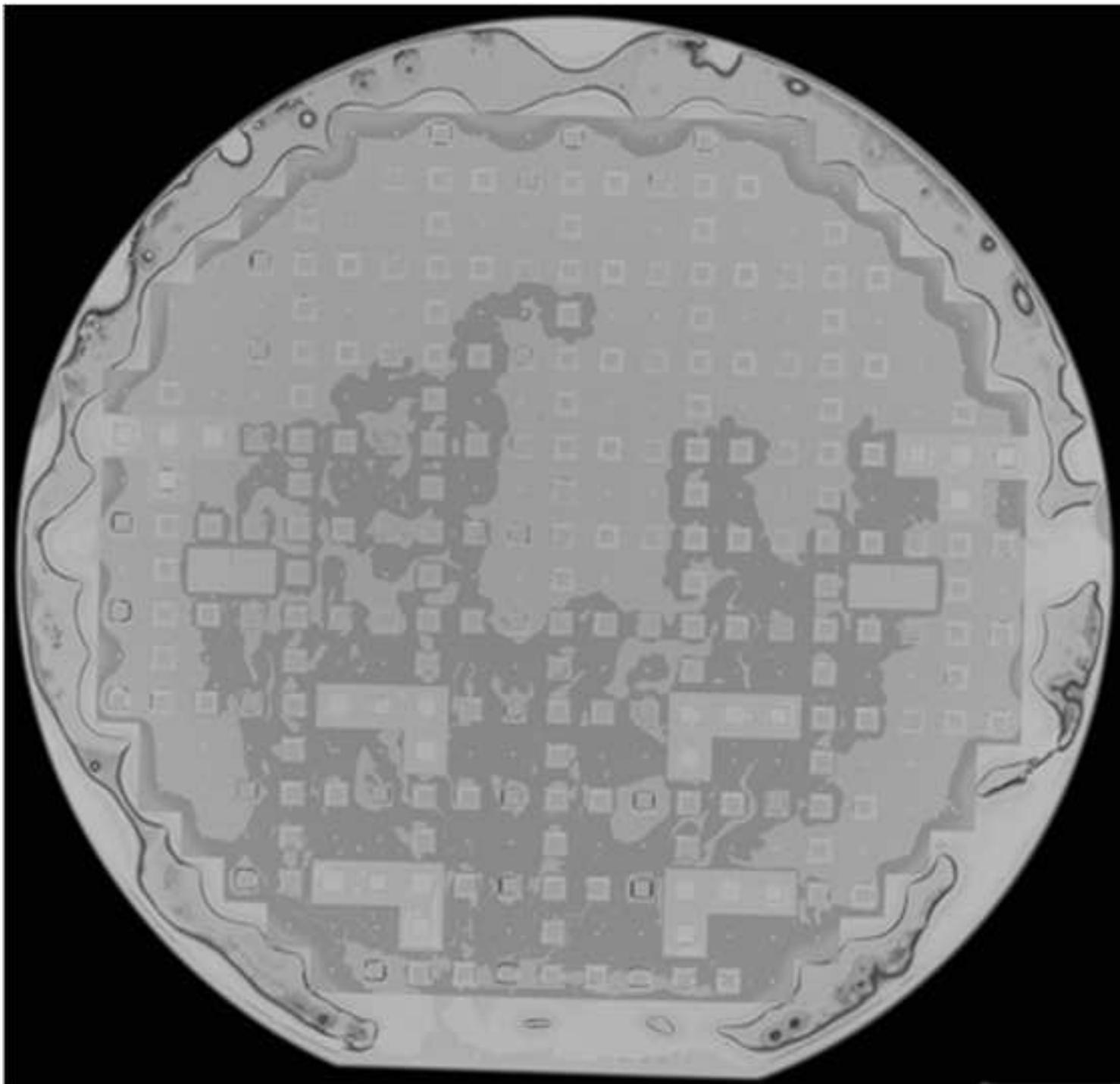
Figure 05
Click here to download high resolution image
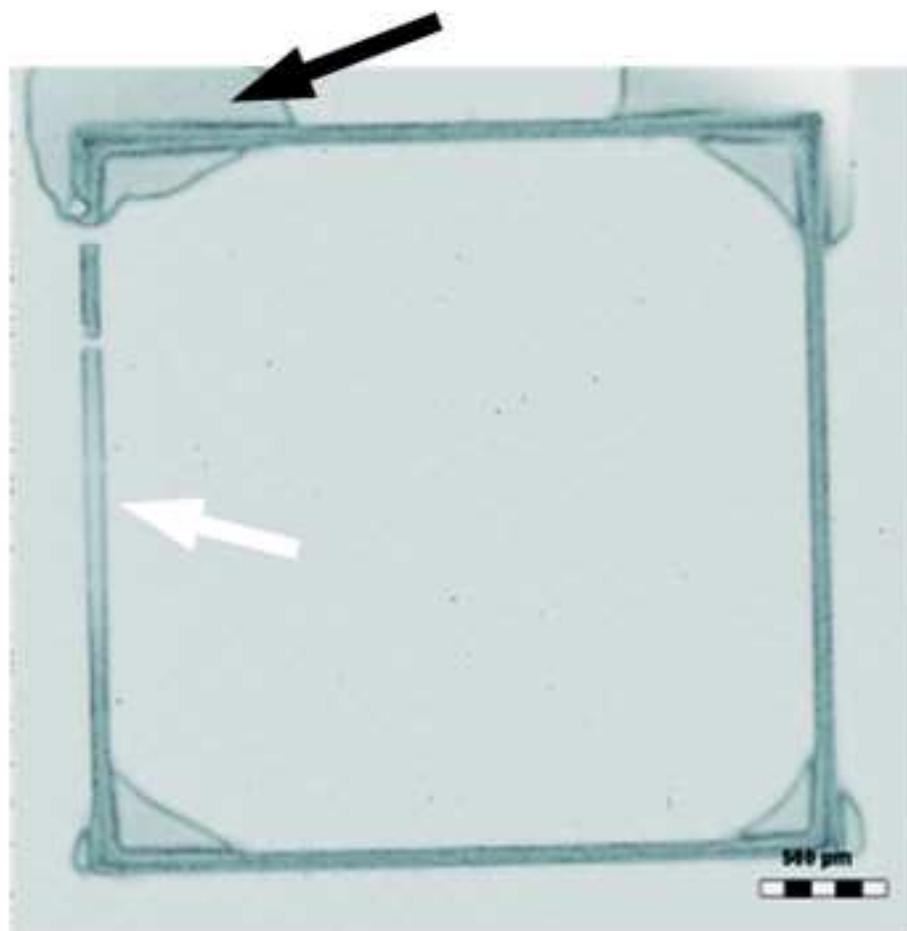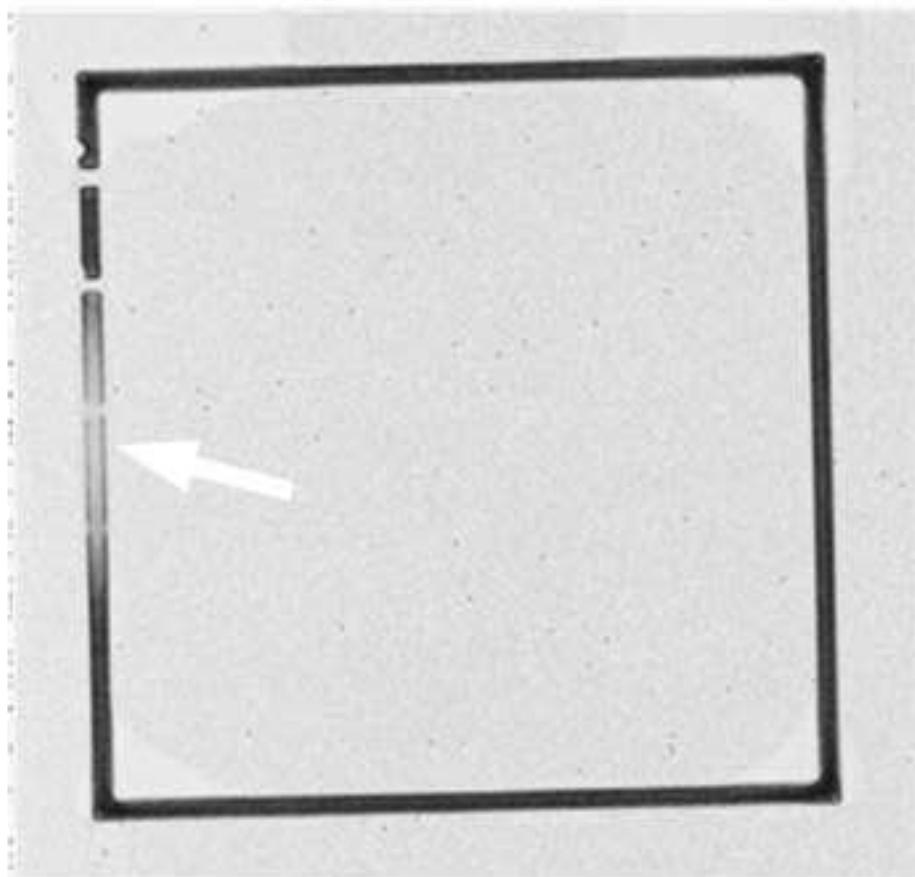
Figure 06
Click here to download high resolution image
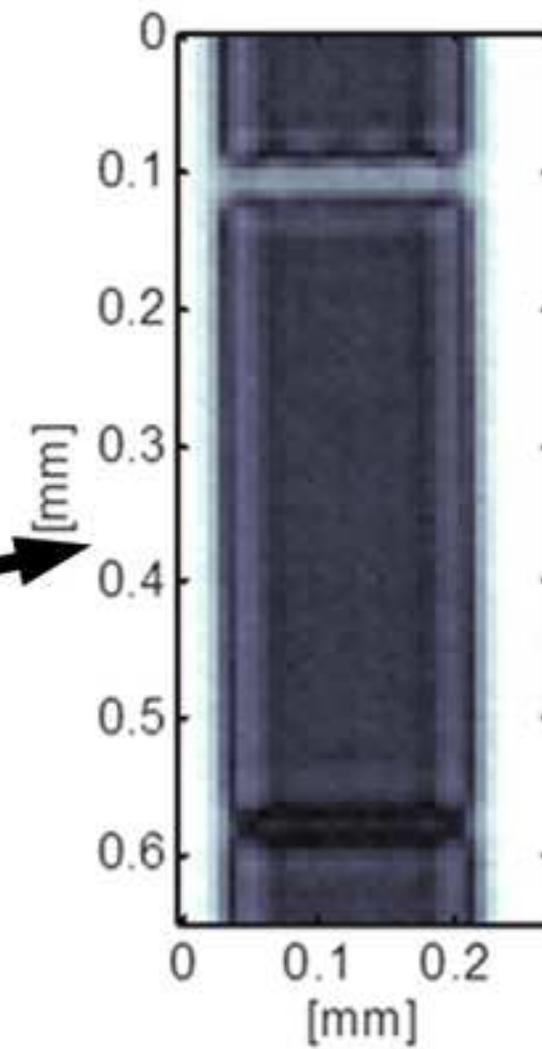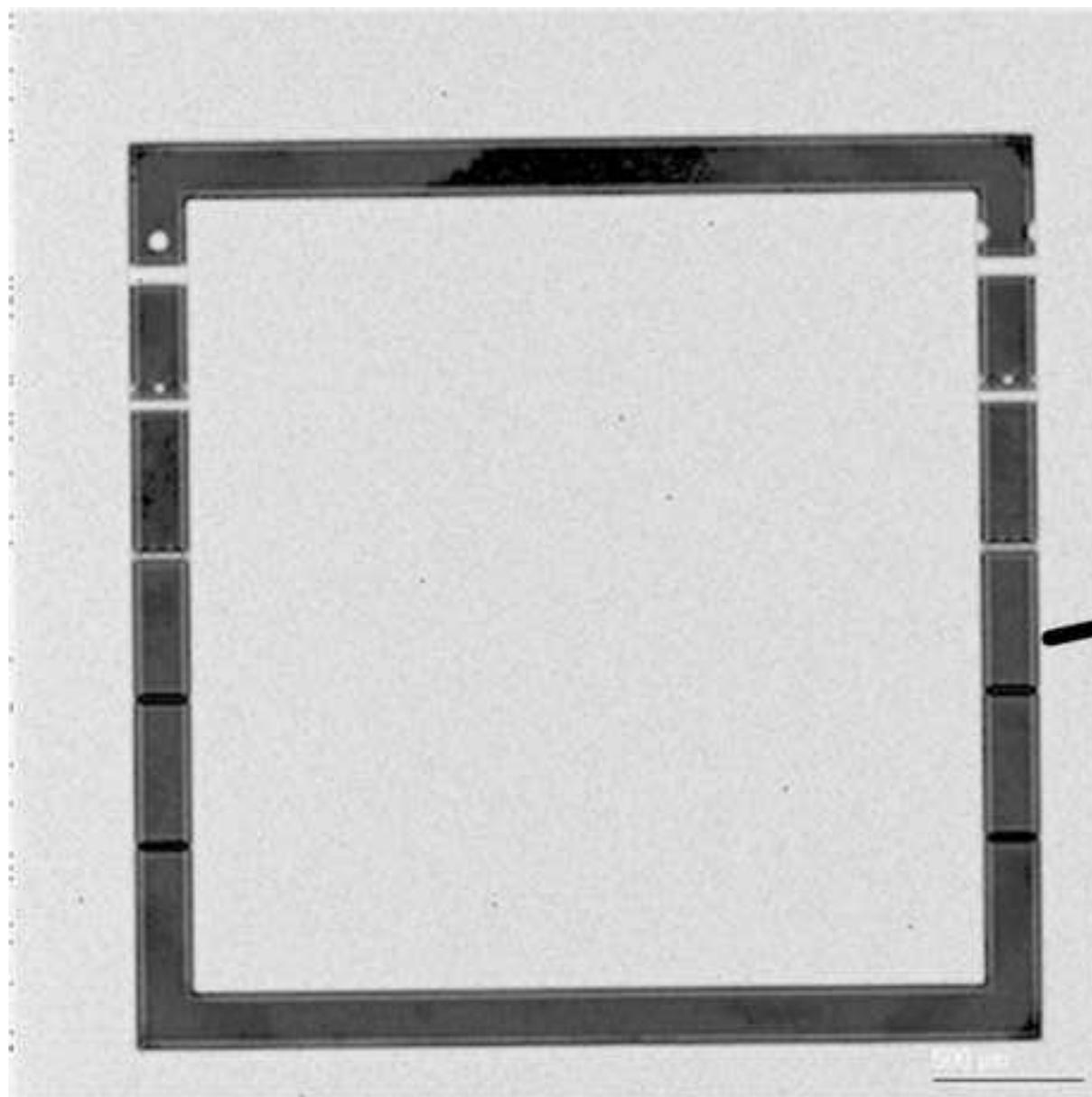
Figure 07
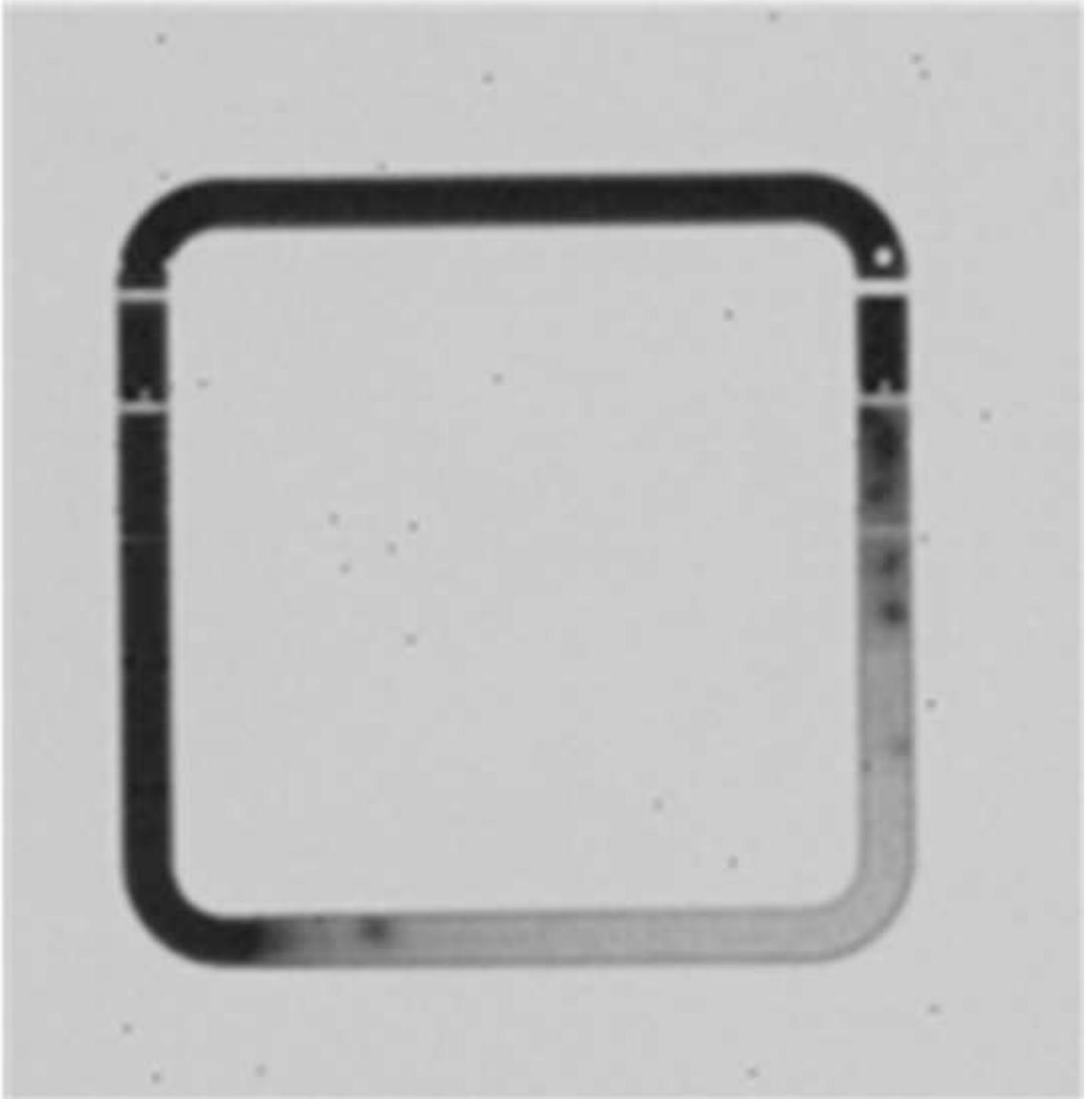
Figure 08
Click here to download high resolution image
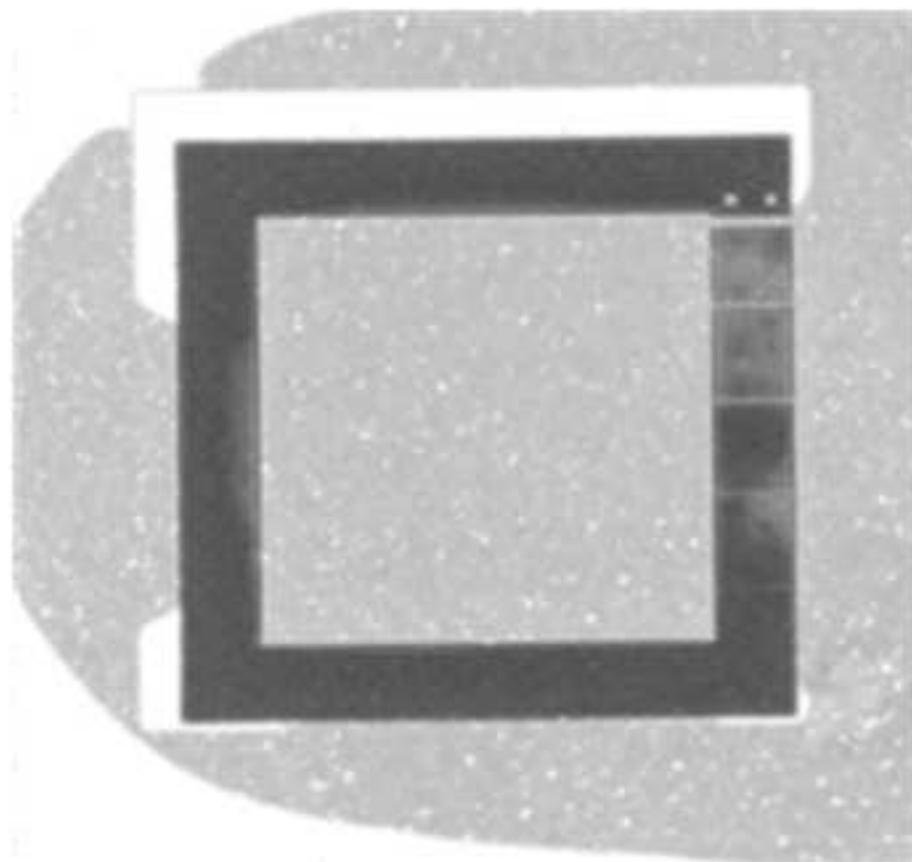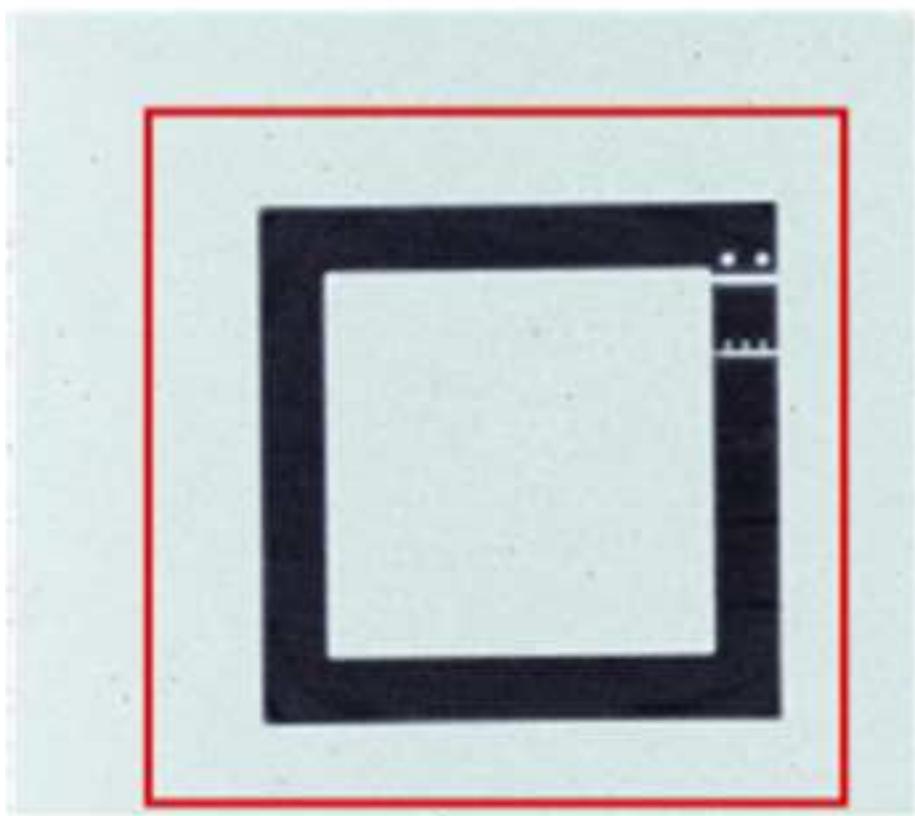
Figure 09
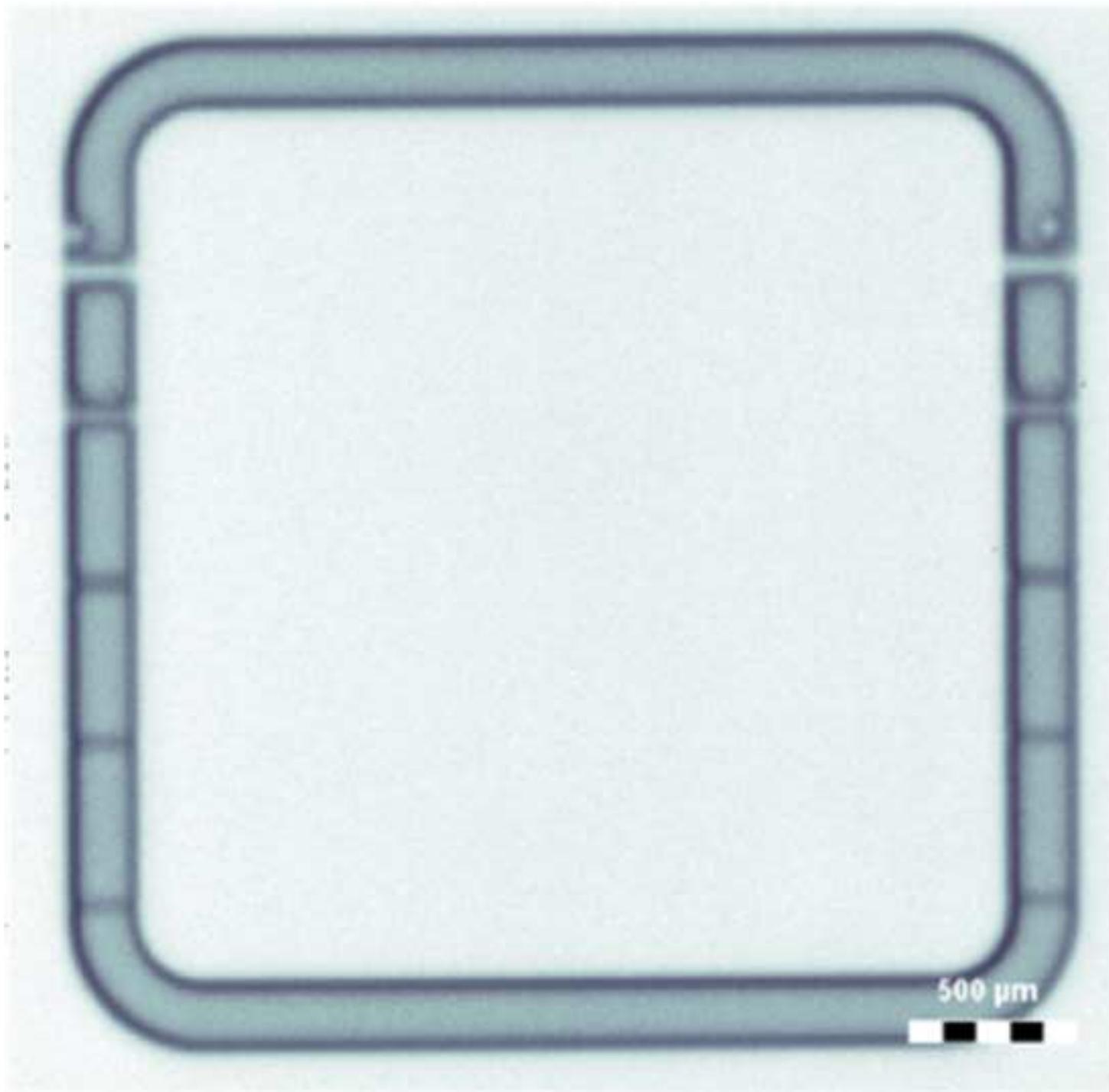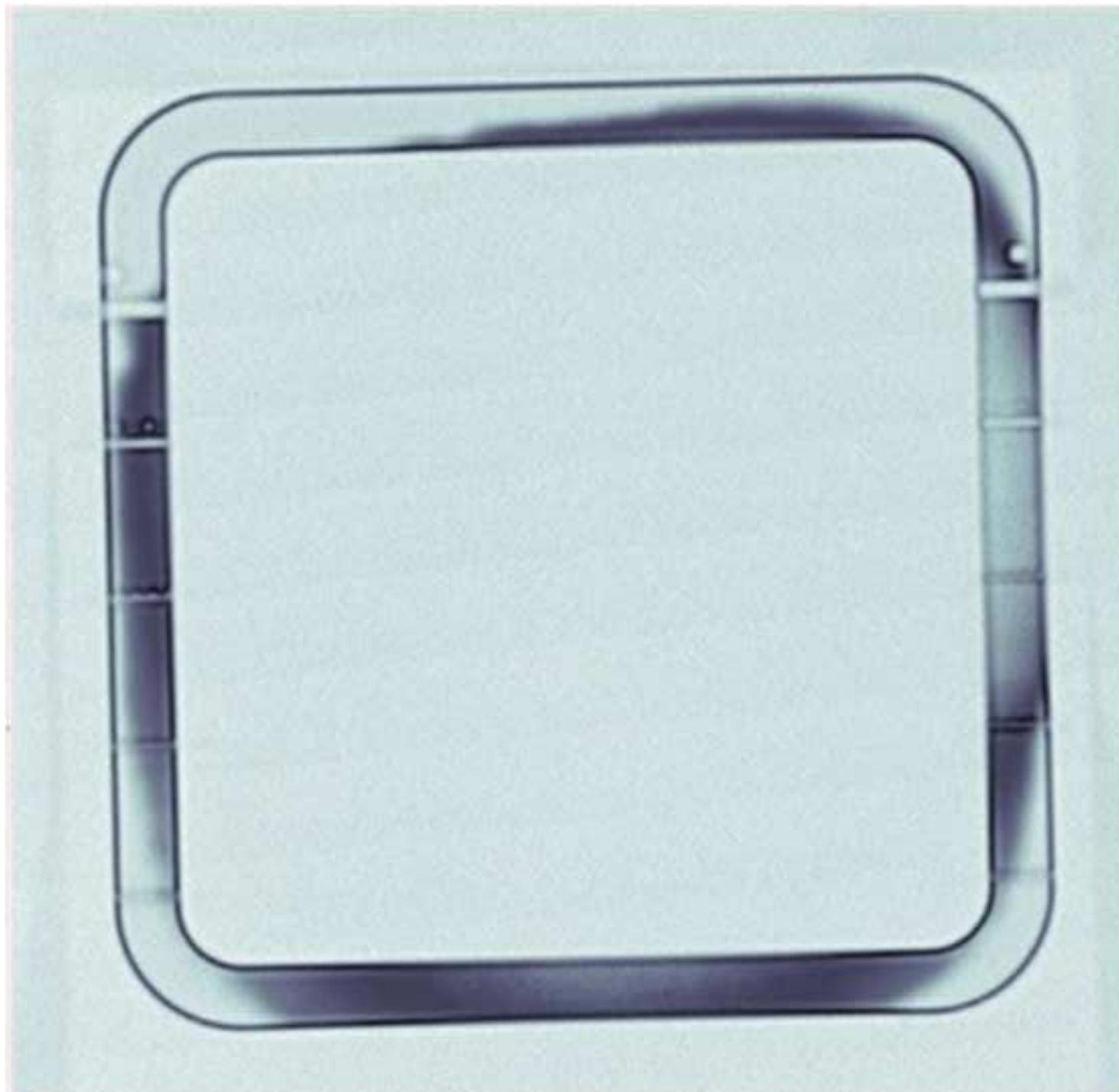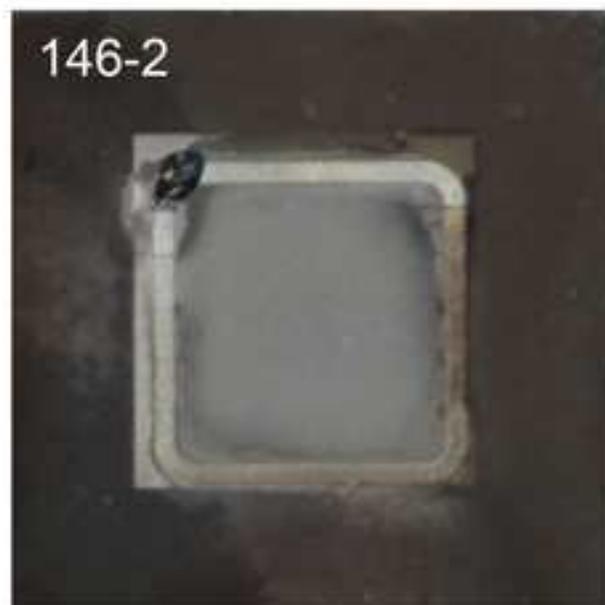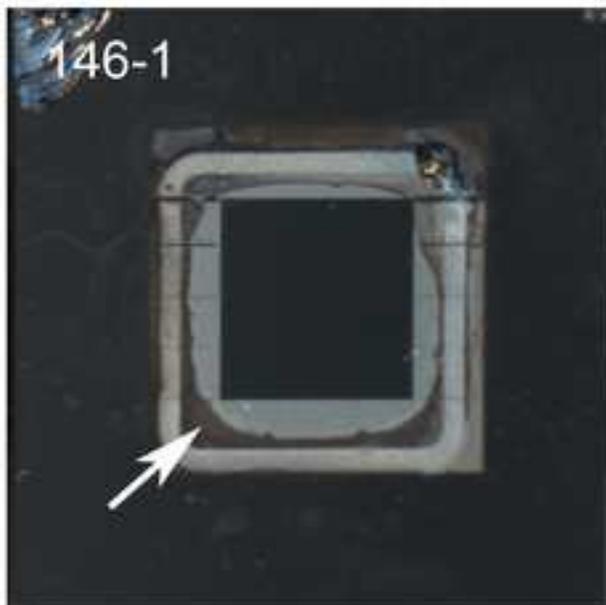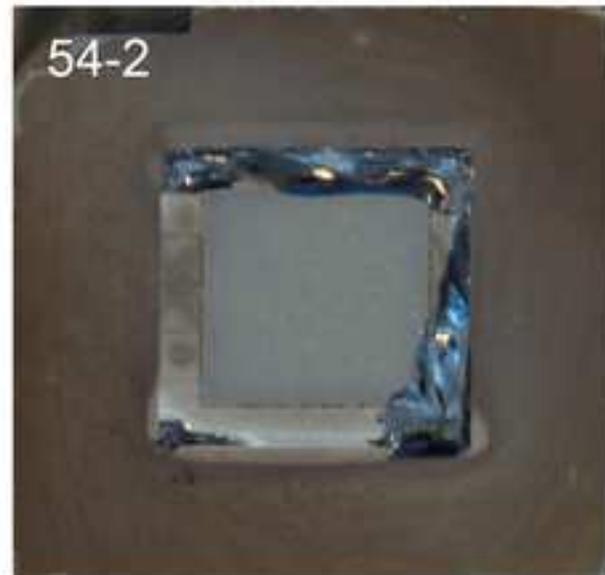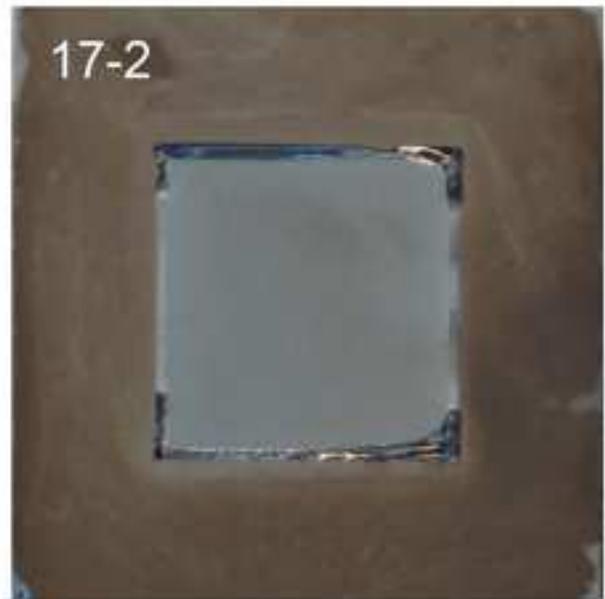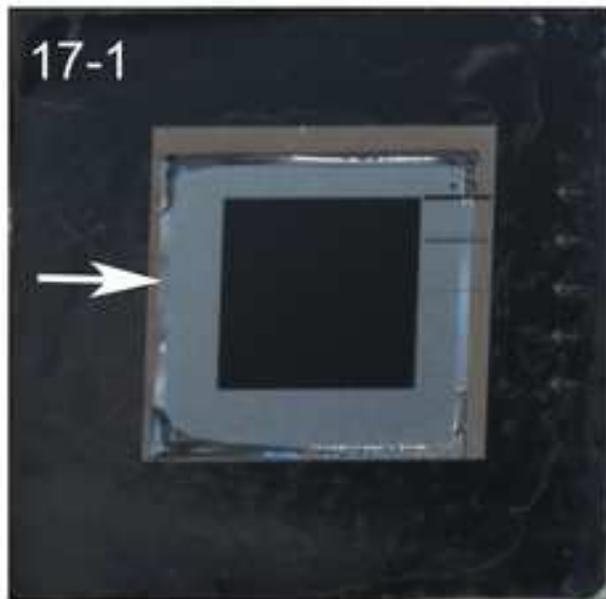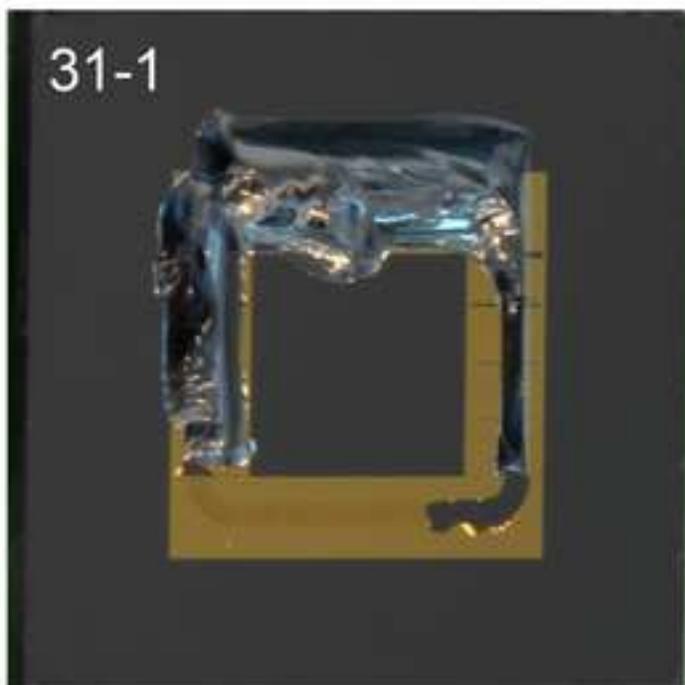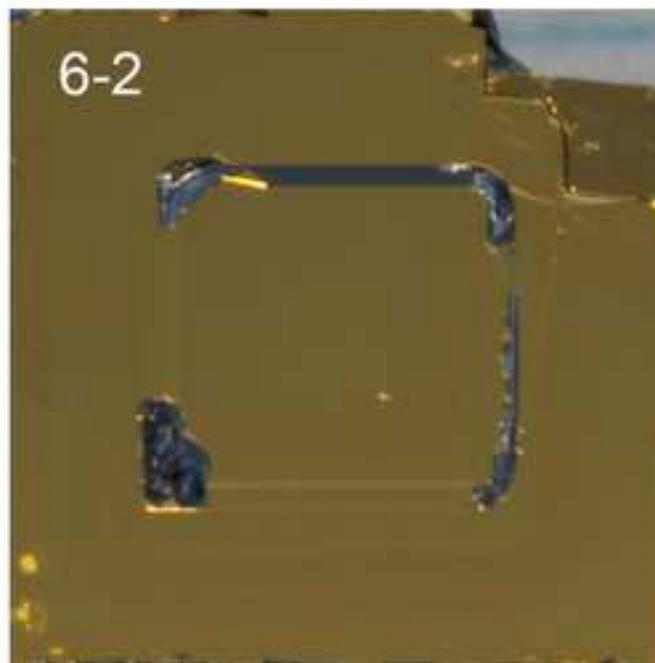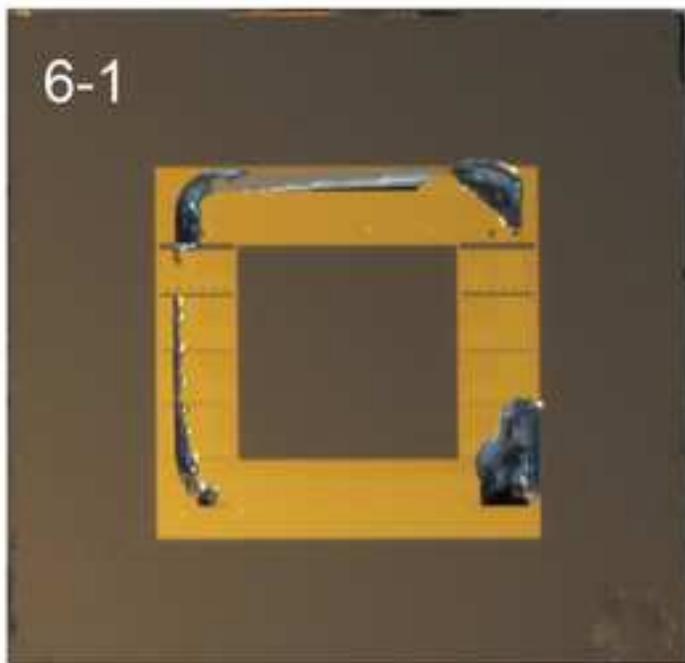
Figure 10

Figure 12

Figure 13
Click here to download high resolution image

pdf file